Ice Porosity Measurement Utilizing Dynamic Wavelet Fingerprint Technology

GUI Kang[1,2], *ZHANG Yabo*[1], *GE Junfeng*[1,2*], *LI Renfu*[3], *YE Lin*[1]

1. School of Artificial Intelligence and Automation, Huazhong University of Science and Technology, Wuhan 430074, P.R.China;

2. Key Laboratory of Icing and Anti/De-icing, China Aerodynamics Research and Development Center, Mianyang 621000, P.R.China;

3. School of Aerospace Engineering, Huazhong University of Science and Technology, Wuhan 430074, P.R.China

(Received 10 March 2023; revised 15 June 2023; accepted 10 August 2023)

Abstract: In order to cope with the problem of ice porosity measurement in aircraft icing scenarios, an ultrasonic porosity measurement method based on dynamic wavelet fingerprint technology is proposed and evaluated. The propagation process of ultrasonic longitudinal waves is analyzed by theoretical model and finite element simulation, and the mechanism of the influence of pore size and other factors on porosity measurement is illustrated. Combined with 60 sets of ultrasonic measurement data of 20 ice samples, wavelet fingerprint images are generated, and 11-D key features are extracted. Based on the principal component analysis and polynomial fitting, the realized porosity measurement root mean square error (RMSE) reached 1.144%, which shows the proposed method is more stable and accurate than the traditional peak fitting method.

Key words: ice porosity measurement; pore distribution; ultrasonic pulse echo; propagation model; dynamic wavelet fingerprint

CLC number: TB551 **Document code:** A **Article ID:** 1005-1120(2023)S1-0118-11

0 Introduction

Icing phenomena are a huge safety hazard for all types of aircraft[1-2]. Even very thin ice growing on avionics surfaces can cause pilots or autopilots to perform fatal misoperations[3-5]. For instance, Air France 447 took 228 lives due to icing on the pitot tube. At the same time, icing on fuselage surfaces will reduce lift-to-drag ratios, increase stall speeds, and threaten engine operation, all of which are particularly deadly for small and medium-sized aircraft[6], as Continental Express Flight 3407 and Florida Flight 90 both crashed due to wing or tail icing, resulting in a large number of air and ground casualties.

Almost all aircraft are equipped with increasingly advanced de-icing systems to cope with icing phenomena[5-7]. To achieve the goal of high energy efficiency, icing detection devices are playing an increasingly indispensable role in these systems. In recent years, many ice detection techniques based on different principles have been developed[8-9], including resonance[10-11], optical fiber[12-14], spectral absorption[15-16], microwave[17], radar[18], impedance[19-22], ultrasound[23-30], etc. These ice sensors are applied in different fields with their own advantages.

The ultrasonic signal describes the relaxation absorption, scattering, and dispersion of acoustic waves in the ice layer, and contains rich information on the morphology, phase, pore distribution, and adhesion of the ice layer[31]. At present, ultrasonic icing detection is mainly divided into two categories, guided-wave detection and pulse-echo measurement. Guided-wave detection is associated with

*Corresponding author, E-mail address: gejf@hust.edu.cn.

How to cite this article: GUI Kang, ZHANG Yabo, GE Junfeng, et al. Ice porosity measurement utilizing dynamic wavelet fingerprint technology[J]. Transactions of Nanjing University of Aeronautics and Astronautics, 2023, 40(S1): 118-128.

http://dx.doi.org/10.16356/j.1005-1120.2023.S1.011

the bottom surface properties of the ice layer, and guided-wave detection array techniques have emerged with better surface detection capability[27-30].

Ultrasonic echoes, on the other hand, are more suitable for measuring the internal structure of ice. Many researchers have studied the acoustic properties of sea ice and proposed empirical formulas for porosity measurements[32], but they are still not sufficient for use in ice measurements on the surface of structures such as aircraft. Liu et al.[23] achieved a preliminary identification of glazed ice and rime ice by means of echo attenuation coefficients and hypothesized that there should be a positive correlation between porosity and frequency characteristics of attenuation coefficients. In 2021, Mendonck et al.[24] confirmed from a measurement perspective that ice porosity is not only associated with attenuation characteristics, but also affects ultrasonic propagation velocity. In 2022, Wang et al.[25] used ultrasonic pulse echoes to conduct an in-depth study of the freezing characteristics of the water film on the ice surface, and accurately measured the thickness of the ice layer and the water film by introducing a transition layer. In the same year, Wang's team[26] proposed the first ultrasonic pulse-echo measurement of ice surface roughness, which achieved the expected results and also illustrated the effect of ice surface morphology on the echo amplitude. Their research results are of great significance to the development of ice growth models.

In order to more accurately identify ice patterns in aircraft icing scenarios, help pilots quickly assess flight conditions, and improve the energy efficiency of anti-icing systems, this paper proposes an ice porosity measurement method using dynamic wavelet fingerprinting techniques. The time-frequency characteristics of the ultrasonic pulse echo signal are analyzed by wavelet decomposition, and the corresponding features are extracted by combining with fingerprint slicing. Through simulation analysis and icing experiments, the advantages of fingerprint features over traditional methods in porosity measurement are evaluated.

1 Ultrasonic Propagation Model

Most of the existing studies employ the peak value of ultrasonic echo for porosity characterization, and this method has been verified to have good feasibility and certain accuracy. In fact, the relationship between porosity and ultrasonic echo is very complex as the acoustic waves need to go through refraction, reflection, scattering and absorption processes in the ice layer. The parameters of the model are listed in Table 1.

Table 1 Relevant parameters of acoustic wave propagation in medium

Medium	Density/ ($g \cdot cm^{-3}$)	Velocity/ ($m \cdot s^{-1}$)
Air	0.012 9	330
Ice	0.918	3 600
Organic glass	1.180	2 670

A typical propagation path of an ultrasonic longitudinal wave in an ice layer is shown in Fig.1(a). By using the Snell's Law and the Zoeppritz's Equation, the results of waveform mode conversion of longitudinal waves at the refraction interface can be obtained. As shown in Fig.1(b) and Fig.1(c), R_L/R_T/S_L/S_T are the normalized amplitudes of reflected and transmitted longitudinal and transverse waves, respectively. When the incident angle is 5°, if the longitudinal wave is incident from the organic glass into the ice layer, the transmitted transverse wave amplitude is only 1.63% of the incident wave. If the longitudinal wave is incident from the ice layer into the organic glass, the transmissive transverse wave amplitude is only 2.44% of the incident longitudinal wave. Therefore, in order to simplify the analytical model of the propagation process of acoustic waves in the medium, the waveform conversion caused by the incident at small angles can be ignored, and the acoustic intensity received by the transducer is composed of the longitudinal reflected acoustic intensity and the transmissive acoustic intensity.

The effect of refraction and reflection on the return amplitude is well defined, and for porosity measurements the propagation of ultrasonic pulses is also influenced by absorption and scattering effects.

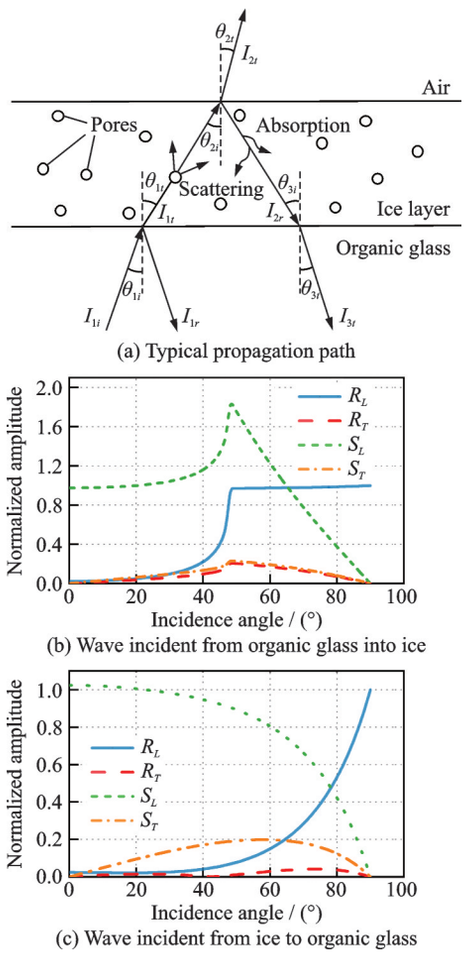

(a) Typical propagation path

(b) Wave incident from organic glass into ice

(c) Wave incident from ice to organic glass

Fig.1 Ultrasonic longitudinal wave propagation modeling and numerical analysis results

According to the boundary conditions of acoustics at the partition interface, the acoustic pressure and the normal mass velocity v_x should be continuous at the $x=0$ position. For a sufficiently small volume element in an acoustic field with medium density ρ and acoustic pressure p, the equation of motion of the medium when there is an acoustic disturbance in the x direction is

$$\rho\frac{\mathrm{d}v_x}{\mathrm{d}t}=-\frac{\partial\rho}{\partial x} \tag{1}$$

Therefore, the velocity v_x of the mass is obtained by integration as follows

$$v_x=-\frac{1}{\rho}\int\frac{\partial p}{\partial x}\mathrm{d}t=\frac{\cos\theta}{\rho c}p \tag{2}$$

where θ is the angle between the direction of acoustic wave propagation and the x-axis, and c the wave speed. From the Sneer's Law, it follows that $\theta_i=\theta_r$, thus obtaining

$$\begin{cases}p_i+p_r=p_t\\ \dfrac{\cos\theta_i}{\rho_1c_1}p_i-\dfrac{\cos\theta_i}{\rho_1c_1}p_r=\dfrac{\cos\theta_t}{\rho_2c_2}p_t\end{cases} \tag{3}$$

where c_1 and c_2 denote the acoustic velocity of the longitudinal wave in the medium. The expression of the acoustic intensity in the medium is given by

$$I=-\frac{p^2}{2\rho c_0} \tag{4}$$

where c_0 is the propagation velocity of the acoustic wave in the medium. On the other hand, because the area of the acoustic beam changes at oblique incidence, the acoustic intensity transmission coefficient does not fully represent the energy relationship of transmission, so the average acoustic energy flow W is introduced, which is the average acoustic energy per unit time through the area S vertical to the direction of acoustic propagation, shown as

$$\begin{cases}r_w=\dfrac{W_\mathrm{r}}{W_\mathrm{i}}=\dfrac{I_\mathrm{r}S_\mathrm{r}}{I_\mathrm{i}S_\mathrm{i}}=\dfrac{r_\mathrm{I}\cos\theta_\mathrm{r}}{\cos\theta_\mathrm{i}}=\\ \qquad\dfrac{\left(\rho_2c_2\cos\theta_\mathrm{i}-\rho_1c_1\cos\theta_\mathrm{t}\right)^2}{\left(\rho_2c_2\cos\theta_\mathrm{i}+\rho_1c_1\cos\theta_\mathrm{t}\right)^2}\\ t_w=\dfrac{W_\mathrm{t}}{W_\mathrm{i}}=\dfrac{I_\mathrm{t}S_\mathrm{t}}{I_\mathrm{i}S_\mathrm{i}}=\dfrac{t_\mathrm{I}\cos\theta_\mathrm{t}}{\cos\theta_\mathrm{i}}=\\ \qquad\dfrac{4\rho_1c_1\rho_2c_2\cos\theta_\mathrm{i}\cos\theta_\mathrm{t}}{\left(\rho_2c_2\cos\theta_\mathrm{i}+\rho_1c_1\cos\theta_\mathrm{t}\right)^2}\end{cases} \tag{5}$$

where the incident acoustic wave cross-sectional area S_i, the reflected acoustic wave cross-sectional area S_r and the transmitted acoustic wave cross-sectional area S_t also comply with the Snell's Law, so the reflection coefficient r_w and the transmission coefficient t_w of the acoustic energy flow can be expressed by the incident energy flow W_i, the reflected energy flow W_r and the transmitted energy flow W_t; r_I is the acoustic intensity reflectance and t_I the acoustic intensity transmittance.

Meanwhile, the energy dissipation in the form of absorption and scattering during acoustic wave propagation can be considered to follow the exponential decay law. In the case of neglecting inelastic scattering, Mie scattering occurs when the ice pore size is comparable to the ultrasonic pulse wavelength, and the attenuation factor is directly related to the pore density and size. Assuming that a path of length Δx in the ice layer is filled with spherical

pores of radius r_3 and spatial density K, and defining the proportion of energy loss due to Mie scattering as Q_S, the total scattering equivalent weakened cross-sectional area σ_S is

$$\sigma_S = Q_S \pi r_3^2 K S_i \Delta x \tag{6}$$

Thus, the total dissipation power of the acoustic wave $P_i(\Delta x)$ is

$$P_i(\Delta x) = P_i(x) - P_i(x + \Delta x) = P_i(x)\frac{\sigma_S}{S_i} = P_i(x) Q_S \pi r_3^2 K \Delta x \tag{7}$$

Therefore, by deriving the differential equation, it can be seen that the acoustic power in the case of considering the scattering effect can be expressed as

$$P_i(x) = P_i e^{-Q_S \pi r_3^2 K x} = P_i e^{-3Q_S R_P x/(4r_3)} \tag{8}$$

where R_P is the porosity calculated based on the spherical pore radius and spatial density. From the derived results, it is clear that for the Mie scattering effect, the porosity and the pore size jointly determine the amplitude of the acoustic power. At the same time, the absorption effect of the ice layer follows the Beer Lambert's Law, and a is the absorption coefficient, shown as

$$I_t = I_i e^{-ax} \tag{9}$$

Therefore, the expression for the echo acoustic power P_S, taking into account the acoustic absorption and scattering effects, is

$$\begin{cases} P_S = P_i\left(r_{W1} + t_{W1} \cdot r_{W2} \cdot t_{W3} e^{-(a_s + a_a)x}\right) \\ a_s = Q_S \pi r_3^2 K x \\ x = \dfrac{2d}{\cos \theta_t} \end{cases} \tag{10}$$

where d is the ice thickness, a_s the scattering attenuation coefficient, and a_a the absorption attenuation coefficient.

Assuming that the ice absorption attenuation coefficient is 0.01 cm^{-1} and the energy loss ratio Q_S caused by Mie scattering is 0.2, the trend of the total reflected acoustic power coefficient C_P of the 3 mm ice layer with the porosity R_P and pore size r_3 is shown in Fig.2. The results of the theoretical model analysis point out that the peak of the ultrasonic echo is roughly exponentially decaying with the rise of the porosity, but it is also influenced by the pore size, the absorption coefficient of the ice layer and other factors. Therefore, the porosity measurement only with reference to the echo peak has certain limitations. On the other hand, in the actual measurement process, the ice surface roughness, phase conditions and other factors also determine the amplitude of the echo peak. Overall, there are many factors associated with the echo peak, which will cause instability of the features in some specific cases and lead to interference of the measurement results.

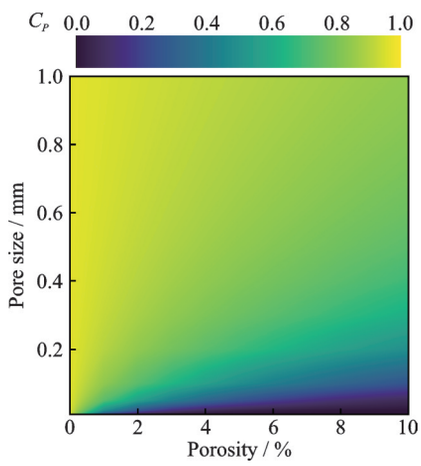

Fig.2 Relationship between total reflected acoustic power coefficient C_P and pore distribution

2 Simulation and Feature Extraction

Based on the theoretical model above, a finite element simulation is performed using the acoustic module of COMSOL multi-physics field simulation software. Modeled according to the form of single-crystal ultrasonic probe, the diameter of the probe delay block is 6 mm, and the thickness of the ice layer above it is set to 2 mm, where the delay block and the ice layer materials are chosen as organic glass and −20 ℃ solid water, respectively. The random porous bubble model is used, and the modeling and meshing results are shown in Fig.3(a) when the porosity is 6%. The physical field is chosen as pressure acoustic, transient module, considering heat conduction and scattering effects. The bottom of the delay block is set as the excitation source, and its center frequency is 10 MHz, as shown in Fig.3(b). Other boundary conditions are set as hard acoustic

field boundary, and the ice layer is coupled with the delay block using consistent boundary pairs and continuity.

The ultrasonic echo simulation results for different porosity ice layers are shown in Fig.3(c). When the pore radius r_3 is in the range of 0.025 mm to 0.05 mm, the time domain signals of 10 MHz ultrasonic longitudinal wave propagation in ice layer with 2 mm thickness are obtained by setting the porosity R_P to 1%, 5% and 9%, respectively. The results indicate that the primary echo peaks of 1%, 5% and 9% porosity ice are 3.62×10^8 Pa, 1.49×10^8 Pa and 0.72×10^8 Pa, respectively, i.e., when the ice thickness and pore radius are comparable, the primary echo signal decays exponentially with the increase of porosity, and the fitted curve R^2 value reaches 0.996, which is consistent with the conclusion in the theoretical model.

To describe the effects of different pore distributions on the ultrasonic echo signals, a random pore model is used to set the porosity to 1%, 5% and 9%, and the pore radius ranges to 0.025—0.05 mm, 0.05—0.1 mm and 0.1—0.2 mm, respectively for the combination of pore distributions. A total of 9 models are created. The data processing of the received echo signals using the time-frequency analysis of dynamic wavelet fingerprints is performed with Morlet complex wavelet basis decomposition, and the wavelet fingerprint images are obtained by equidistant slicing. Typical images of medium and large size pore models are shown in Figs.4 (a—f). As shown in Fig.4(b), the upper boundary longitudinal coordinate Y_1 of the fingerprint is obtained by graying out and calculating the connected domain of the wavelet fingerprint image, and the pore distribution information is characterized together with the primary echo peak acoustic pressure P_{peak}. By randomly changing the pore coordinates for each pore distribution, three sets of simulation experiments are conducted to obtain the relationship between pore distribution and two features. The exponential function is used to fit the feature results,

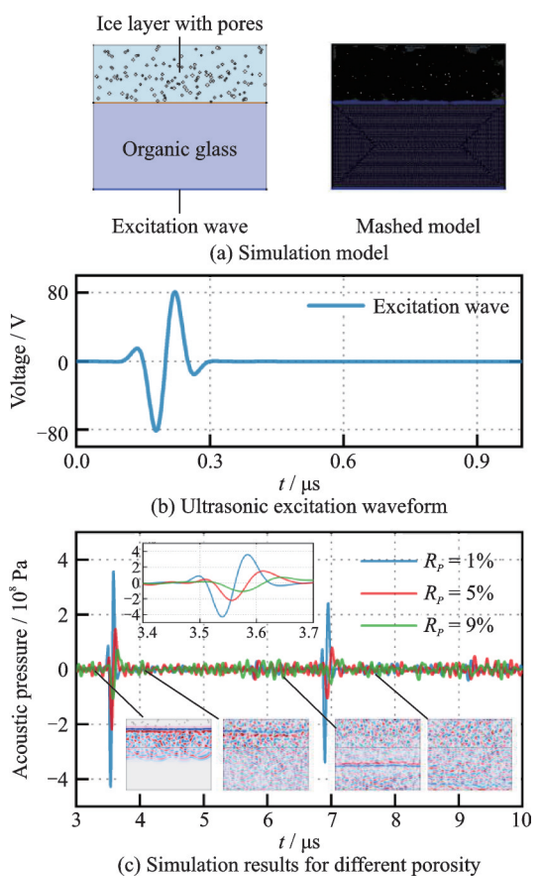

Fig.3 Ultrasonic ice detection model and finite element analysis results

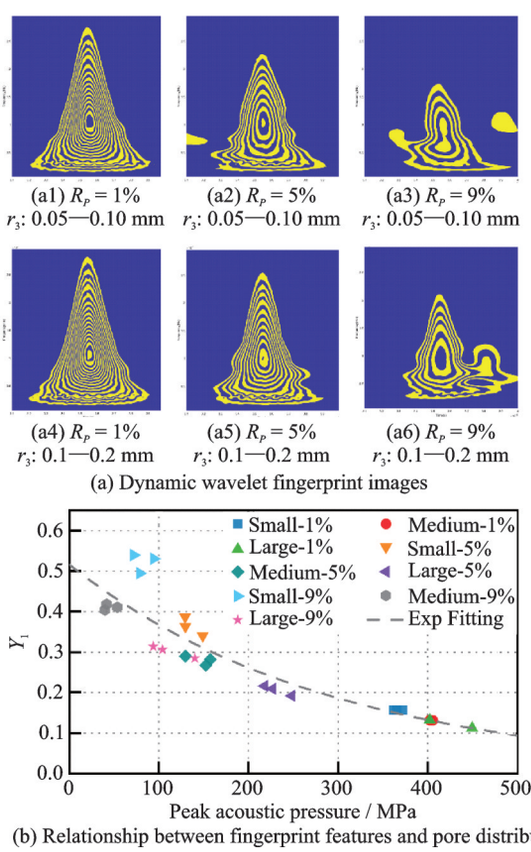

Fig.4 Dynamic wavelet fingerprint images and characteristics of ultrasonic echoes with different pore distributions

and the results show that the pore distribution has a strong correlation with the primary echo peak acoustic pressure P_{peak} and the fingerprint upper boundary longitudinal coordinate Y_1, and with the increase of porosity and pore radius, Y_1 becomes larger and P_{peak} decreases.

Obviously, the peak of the primary echo is still a very important feature, but not the only one. In the actual measurement scenario, the peak amplitude is easily disturbed, but the overall waveform of the ultrasonic echo is relatively stable. Therefore, by extracting wavelet fingerprint image features, the stability of porosity measurement can be effectively improved.

3 Experiment Setup

The ultrasonic longitudinal wave ice detection experimental platform is designed according to the above theory and simulation model, including pulse signal generator, ultrasonic probe and high-precision constant temperature experimental chamber and other equipment, and the platform is built, as shown in Fig.5(a). The excitation voltage of the signal generator is set to −50 V, and the probe is selected as a single crystal longitudinal wave straight probe with a measured center frequency of 6 MHz.

In the experiments, the ambient temperature is −12 ℃ and the icing thickness is 3 mm. A total of 60 measurements were performed on 20 ice samples, which are grouped as shown in Table 2. The true values of porosity in the table are obtained by

Table 2 Grouping of icing experimental data

Group	Ice sample	Case number	Porosity range/ %
Low porosity & small bubbles	1—4	1—10	0—0.97
Low porosity & large bubbles	5—7	11—18	0.75—2.02
Medium porosity & small bubbles	8—9	19—26	1.8—2.2
Medium porosity & large bubbles	10—14	27—38	1.21—5.05
High porosity & small bubbles	15—17	39—50	5.17—8.59
High porosity & large bubbles	18—20	51—60	6.99—13.93

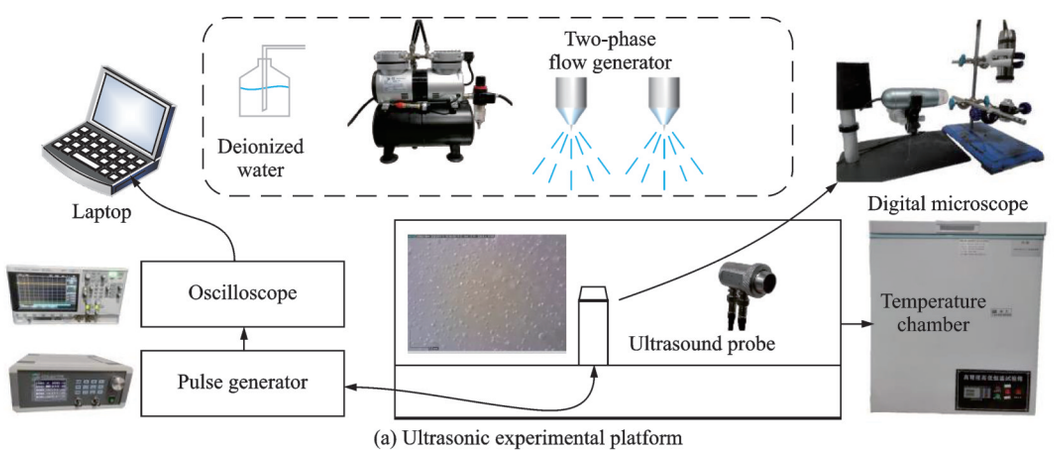

(a) Ultrasonic experimental platform

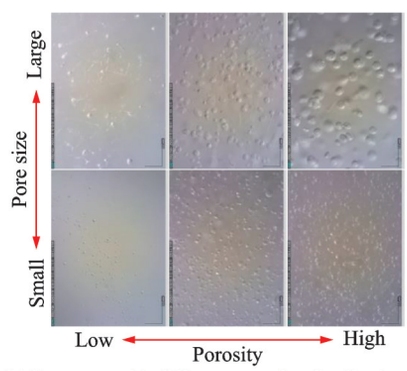

(b) Ice types with different porosity distributions

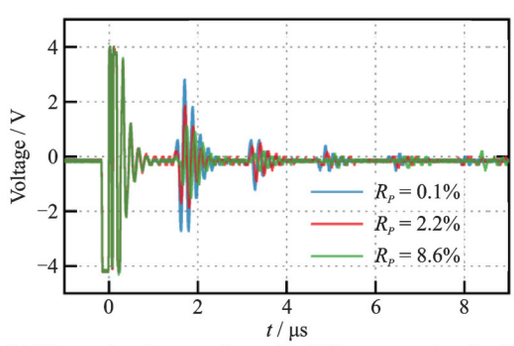

(c) Ultrasonic echo waveform with different pore size distributions

Fig.5 Experimental setup for ultrasonic icing detection and some results

means of image processing. The bubble size statistics in the digital microscope images indicate the value of the ice pore volume ratio, and stable porosity results are obtained by averaging over multiple acquisitions. The pictures of ice samples with different porosity and pore size are shown in Fig.5(b), and partial ultrasonic signals corresponding to the case of average pore size less than 100 μm are shown in Fig.5(c).

4 Results and Discussion

Dynamic wavelet fingerprint image extraction is conducted on the ultrasound echo data. Morlet complex wavelet basis decomposition is employed to obtain fingerprint images by equidistant slicing as shown in Fig.6. The typical fingerprint images of different groups have obvious differences in fingerprint complexity and shape contour. Feature extraction is performed for these differences, and the feature definitions and their Pearson correlation coefficients are shown in Table 3.

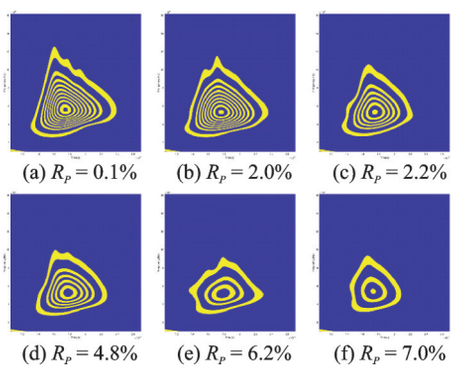

Fig.6 Typical fingerprint images of ice samples with different porosity

Table 3 Feature definitions and Pearson correlation coefficients

Feature	Description	Pearson correlation coefficient
Peak	Primary echo peak voltage	−0.82
Convex area	Minimum convex polygon area of fingerprint image	−0.80
External rectangular area	Minimum external rectangular area of fingerprint image	−0.80
Equivalent diameter	Diameter of the circle with the same area as the convex polygon of the fingerprint image	−0.79
Elliptic short axis	The length of the short axis of the ellipse with the same normalized second-order central moment as the fingerprint image	−0.67
Elliptic long axis	The length of the long axis of the ellipse with the same normalized second-order central moment as the fingerprint image	−0.82
Minimum Feret diameter	The minimum distance between any two boundary points of the convex polygon that encloses the fingerprint image	−0.81
Maximum Feret diameter	The maximum distance between any two boundary points of the convex polygon that encloses the fingerprint image	−0.68
Centroid X	The horizontal coordinate of the centroid of the fingerprint image	−0.18
Centroid Y	The vertical coordinate of the centroid of the fingerprint image	0.83
Y_1	Fingerprint image upper boundary vertical coordinate	0.84
Y_2	Fingerprint image lower boundary vertical coordinate	−0.60
Lateral span	Fingerprint image lateral span	−0.60
Vertical span	Fingerprint image vertical span	−0.83
Fingerprint number	Number of fingerprint ridges	−0.81

The 11-D features with correlation coefficients higher than 0.75 with respect to porosity are selected for principal component analysis (PCA), and the results are shown in Fig.7. Based on the PCA results, the first two principal components explained more than 97% of the variance. Therefore, the first two principal components are chosen as features to fit polynomial surfaces for the porosity measurement.

In the traditional method, the peak value is used as the only characterization of porosity. As shown in Table 3, the correlation coefficient between peak value and porosity is only 0.82 due to factors such as ice surface roughness, pore size, and ice absorption coefficient, which will lead to a large error in porosity measurement. According to the ex-

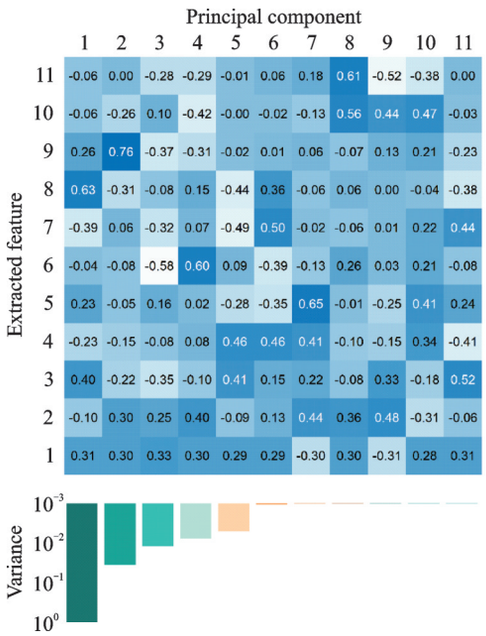

Fig.7 Results of principal component analysis of 11-D features

perimental results, the R^2 value of the fitted exponential curve for the peak data is only 0.754 2 and the root mean square error (RMSE) is 1.503%, while the R^2 value of the fitted quadratic polynomial curve is only 0.796 1 and the RMSE is reduced to 1.381%, as shown in Fig.8(a). A quadratic polynomial fit using the better features in the fingerprint image, such as Y_1, resulted in an R^2 value of 0.752 1 and an RMSE of 1.509%. When a binary cubic surface fit is performed using two principal components, a small improvement is achieved with an R^2 value of 0.877 3 and an RMSE of 1.144%, as shown in Fig.8(b).

In the ultrasonic echo measurement, the peak amplitude is sensitive to the influence of ice structure and chance factors. However, the fingerprint image reflects the time-frequency behavior of the whole echo curve, which has the characteristics of relative stability. Therefore, by extracting features from the fingerprint image, it helps to make up for the shortcomings of the peak in terms of stability.

The results of two ultrasonic measurements of the same ice sample (Ice sample #19), Case 56 and Case 57, are shown in Fig.9. The first measurement involved a small amount of burr on the ice surface, which is relatively rough. The burrs on the ice surface are melted by using a flattening mold before

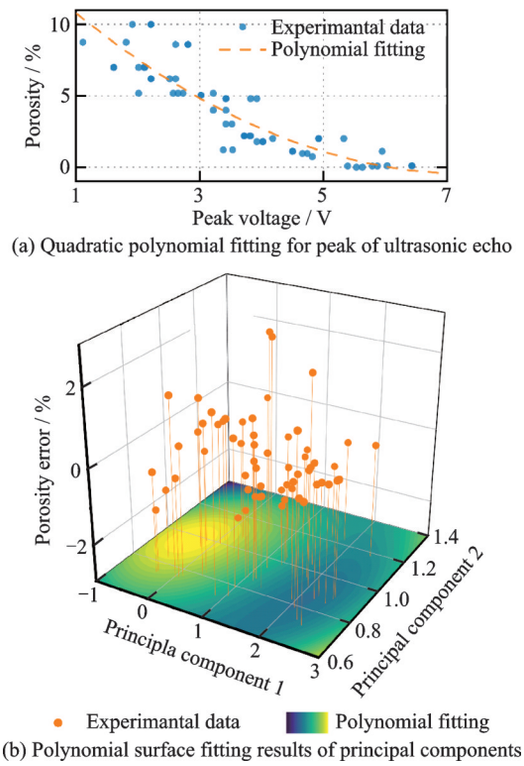

(a) Quadratic polynomial fitting for peak of ultrasonic echo

(b) Polynomial surface fitting results of principal components

Fig.8 Porosity measurements from peak fitting and wavelet fingerprint analysis

the second measurement, resulting in a significant increase in the peak value, and the peak difference between the two measurements reaches 38.6%. By calculating the porosity utilizing the ultrasonic echo peak, then the two measurement results are 7.10% and 9.40%, respectively, and the true porosity label is 8.75%, so the measurement error reaches 19.0% and 7.3%. The conventional method is difficult to meet the application requirements of porosity measurement in terms of accuracy and stability when dealing with the peak instability.

When fingerprint image features as well as peak value are introduced for porosity characteriza-

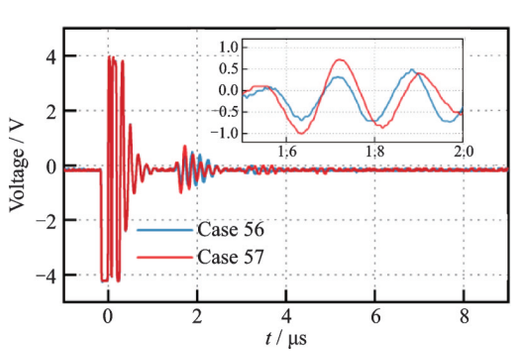

Fig.9 Ultrasonic echo curves obtained from two measurements of Ice sample #19

tion and two principal components are employed for surface fitting, the results of the two measurements are 8.64% and 8.22%, respectively. The true porosity label is 8.75% (Measured by digital microscope and calculated based on the volume ratio of the pores) and the measurement error is 1.3% and 6.1%. The results are significantly better than the peak characterization method.

The method of fitting surfaces by dynamic wavelet fingerprint features to a certain extent reduces the influence brought by peak variations on porosity measurements, but still cannot obtain sufficiently low R^2 values and RMSE values. On the one hand, it is more difficult to obtain the true value of ice porosity, and it must be assumed that there is a large uncertainty in the porosity label data, which also leads to the expansion of the error of measurement results between the traditional and the proposed method in this study. On the other hand, the proposed method still cannot fundamentally solve the measurement problems caused by ice structural parameters such as ice roughness and pore size. Decoupling porosity from key structural factors such as pore size at the feature level is the only way to achieve more stable and accurate porosity measurement results. At the same time, the data set involved in this study needs to be expanded. With the support of sufficient data, regression models using algorithms such as SVR will be considered to obtain more accurate porosity measurements.

5 Conclusions

This research work goes one step further on the basis of the previous research on ice porosity measurement utilizing echo peaks. In this paper, the propagation process of ultrasonic longitudinal waves in ice is analyzed, and the influence mechanism of pore structure on porosity measurement is clarified by constructing a quantitative model and finite element simulation, and a porosity measurement method based on dynamic wavelet fingerprint technology is proposed. The porosity characterization using fingerprint image features can effectively reduce the influence of peak variations on porosity measurement, but still cannot obtain ideal measurement results. The experimental data show that the RMSE of the method reaches 1.144%, which has some advantages over the traditional method, and the main source of error may be the difference of pore size and surface roughness under the same porosity. On the other hand, the nonlinear effect of ice pores can also be characterized by wavelet fingerprint images, so it is promising to decouple the pore size factor and realize the measurement of pore distribution by this method. The iterative work will be carried out around the measurement of ice pore distribution in order to obtain the ice structure parameters more accurately and quickly.

References

[1] PAN R, ZHANG H, ZHONG M. Triple-scale superhydrophobic surface with excellent anti-icing and ice phobic performance via ultrafast laser hybrid fabrication[J]. ACS Applied Materials and Interfaces, 2021, 13(1): 1743-1753.

[2] SHEN H, LI Y, GUO W, et al. Experimental research on adhesion strength of ice accretion on leading edge of symmetric airfoil[J]. Transactions of Nanjing University of Aeronautics and Astronautics, 2023, 40(2): 230-238.

[3] NONG L, XIAN J, HU Z, et al. Analysis of ice-shaped surface roughness based on fractal theory[J]. Transactions of Nanjing University of Aeronautics and Astronautics, 2023, 40(2): 169-178.

[4] ZHONG F, WEI Z, CHEN J, et al. Dynamic behavior and heat transfer characteristics of non-spherical ice crystals in high-temperature air flow[J]. Transactions of Nanjing University of Aeronautics and Astronautics, 2023, 40(2): 205-215.

[5] WANG J, YU D, YANG Z, et al. Experimental investigation of super-hydrophobic / electro-thermal synergistically anti-icing / de-icing strategy in ice wind tunnel[J]. Transactions of Nanjing University of Aeronautics and Astronautics, 2023, 40(2): 193-204.

[6] CAO Y, TAN W, WU Z. Aircraft icing: An ongoing threat to aviation safety[J]. Aerospace Science and Technology, 2018, 75: 353-385.

[7] MORITA K, KIMURA S, SAKAUE H. Hybrid system combining ice-phobic coating and electrothermal heating for wing ice protection[J]. Aerospace, 2020, 7(8): 102.

[8] WEI K, YANG Y, ZUO H, et al. A review on ice

detection technology and ice elimination technology for wind turbine[J]. Wind Energy, 2020, 23(3): 433-457.

[9] MADI E, POPE K, HUANG W, et al. A review of integrating ice detection and mitigation for wind turbine blades[J]. Renewable and Sustainable Energy Reviews, 2019, 103: 269-281.

[10] GUI K, GE J, YE L, et al. The piezoelectric road status sensor using the frequency scanning method and machine-learning algorithms[J]. Sensors and Actuators A: Physical, 2019, 287: 8-20.

[11] ZHANG X, ZHOU W, LI H. Electromechanical impedance-based ice detection of stay cables with temperature compensation[J]. Structure Control and Health Monitoring, 2019, 26: e2384.

[12] AMOIROPOULOS K, KIOSELAKI G, KOURKOUMELIS N, et al. Shaping beam profiles using plastic optical fiber tapers with application to ice sensors[J]. Sensors-Basel, 2020, 20(9): 2503.

[13] GE J, LIU J, GUI K, et al. Atmospheric icing measurement and online ice type recognition for aircraft utilizing optical fiber sensor and machine learning algorithms[J]. Measurement, 2022, 205: 112215.

[14] SIEGL A, NEUMAYER M, BRETTERKLIEBER T. Fibre optical ice sensing: Sensor model and icing experiments for different ice types[C]//Proceedings of the 2020 IEEE International Instrumentation and Measurement Technology Conference (I2MTC). Dubrovnik, Croatia: IEEE, 2020.

[15] JONSSON P, CASSELGREN J, THORNBERG B. Road surface status classification using spectral analysis of NIR camera images[J]. IEEE Sensors Journal, 2015, 15(3): 1641-1656.

[16] ZHANG X, YUE Y, HAN L, et al. River ice monitoring and change detection with multi-spectral and SAR images: Application over yellow river[J]. Multimedia Tools and Applications, 2021, 80: 28989-29004.

[17] KOZAK R, WILTSHIRE B D, KHANDOKER M, et al. Modified microwave sensor with a patterned ground heater for detection and prevention of ice accumulation[J]. ACS Applied Materials and Interfaces, 2020, 12(49): 55483-55492.

[18] BYSTROV A, HOARE E, TRAN T Y, et al. Automotive system for remote surface classification[J]. Sensors-Basel, 2017, 17(4): 745.

[19] NAMPOOTHIRI K N, BOBJI M S, SEN P. De-icing device with self-adjusting power consumption and ice sensing capabilities[J]. Journal of Microelectromechanical Systems, 2020, 29(4): 562-570.

[20] ELZAIDI A, MASEK V, BRUNEAU S. Marine icing sensor with phase discrimination[J]. Sensors, 2021, 21(2): 612.

[21] MARKUS N, THOMAS B, MATTHIAS F. Signal processing for capacitive ice sensing: electrode topology and algorithm design[J]. IEEE Transactions on Instrumentation and Measurement, 2019, 68(5): 1458-1466.

[22] GUI K, LIU J, GE J, YE L. Atmospheric icing process measurement utilizing impedance spectroscopy and thin film structure[J]. Measurement, 2022, 202: 111851.

[23] LIU Y, BOND L J, HU H. Ultrasonic-attenuation-based technique for ice characterization pertinent to aircraft icing phenomena[J]. AIAA Journal, 2017, 55(5): 1-8.

[24] MENDONCK M, APARICIO S, DÍAZ C G, et al. Ultrasonic propagation in liquid and ice water drops. Effect of Porosity[J]. Sensors-Basel, 2021, 21(14): 4790.

[25] WANG Y, WANG Y, WEN L, et al. Study on freezing characteristics of the surface water film over glaze ice by using an ultrasonic pulse-echo technique[J]. Ultrasonics, 2022, 126: 106804.

[26] WANG Y, ZHANG Y, WANG Y, et al. Quantitative measurement method for ice roughness on an aircraft surface[J]. Aerospace, 2022, 9: 739.

[27] ZHAO X, ROSE J L. Ultrasonic guided wave tomography for ice detection[J]. Ultrasonics, 2016, 67: 212-219.

[28] MOLL J, SIMON J, MEMMOLO V. Surface ice detection on composite plates with ultrasonic guided waves[C]//Proceedings of 2019 IEEE 5th International Workshop on Metrology for AeroSpace (MetroAeroSpace).[S.l.]: IEEE, 2019.

[29] MENDIG C, RIEMENSCHNEIDER J, MONNER H P, et al. Ice detection by ultrasonic guided waves[J]. CEAS Aeronautical Journal, 2018, 9: 405-415.

[30] TIAN Y, WANG Q, LIU M, et al. Robust and quantitative characterization of aircraft icing with mode and frequency selective ultrasonic guided wave[J]. Ultrasonics, 2023, 127: 106846.

[31] HOBBS P V. Ice physics[M]. Oxford, UK: Oxford University Press, 2010.

[32] MAKSIMOV A. Acoustic manifestations of frozen bubbles[J]. The Journal of the Acoustical Society of America, 2013, 133(5): 3399.

Acknowledgements This work was funded by the Key Laboratory of Icing and Anti/De-icing of CARDC (No. IADL 20210202). The authors wish to thank Ms. Ivy and the anonymous reviewers for their valuable comments and suggestions which lead to an improvement of this paper.

Authors Dr. **GUI Kang** received the B.S. degree in measurement and control technology and instrumentations from Huazhong University of Science and Technology, Wuhan, Hubei, China, in 2013. He also received the Ph.D. degree in control science and engineering from there in 2019. His research interests are in icing process detection and deicing method.

Dr. **GE Junfeng** received the B.S. degree in measurement and control technology and instrumentations from Huazhong University of Science and Technology, Wuhan, Hubei, China, in 2003. He received the M.S. and Ph.D. degrees in control science and engineering from Tsinghua University, Beijing, China, in 2005 and 2009, respectively. He is currently an associate professor with the School of Artificial Intelligence and Automation, Huazhong University of Science and Technology. His research interests include ice detection, pattern recognition and instrumentation.

Author contributions Dr. **GUI Kang** designed the study, supervised the programming of the data processing algorithms, conducted the data analysis, interpreted the results, and wrote the manuscript. Mr. **ZHANG Yabo** established the theoretical model and simulation model, conducted icing experiments, and contributed to both experimental data and algorithm code. Dr. **GE Junfeng** guided the experimental and analytical process and contributed to the discussion of the study. Prof. **LI Renfu** contributed to the discussion and background of the study, and he also supervised the study. Prof. **YE Lin** supervised the study. All authors commented on the manuscript draft and approved the submission.

Competing interests The authors declare no competing interests.

(Production Editor: SUN Jing)

基于动态小波指纹的冰孔隙率测量方法研究

桂 康[1,2], 张亚博[1], 葛俊锋[1,2], 李仁府[3], 叶 林[1]

(1.华中科技大学人工智能与自动化学院,武汉 430074,中国; 2.中国空气动力研究与发展中心结冰与防除冰重点实验室,绵阳 621000,中国; 3.华中科技大学航空航天学院,武汉 430074,中国)

摘要:针对飞机结冰情况下的冰孔隙率测量问题,提出并评估了一种基于动态小波指纹技术的超声波孔隙率测量方法。通过理论模型和有限元仿真分析了超声纵波的传播过程,阐述了孔隙大小等因素对孔隙率测量的影响机理。结合20块冰样品的60组超声波测量数据,生成了小波指纹图像,并提取了11维关键特征。基于主成分分析和多项式拟合,所实现的孔隙率测量均方根误差(Root mean square error, RMSE)达到1.144%,说明本文方法比传统的峰值拟合方法更稳定、准确。

关键词:冰孔隙率测量;孔隙分布;超声脉冲回波;传播模型;动态小波指纹